Near-*N* Oscillations and Deep-Cycle Turbulence in an Upper-Equatorial Undercurrent Model

HIEU T. PHAM, SUTANU SARKAR, AND KRAIG B. WINTERS

Department of Mechanical and Aerospace Engineering, and Scripps Institution of Oceanography, University of California, San Diego, La Jolla, California

(Manuscript received 15 December 2011, in final form 13 June 2012)

ABSTRACT

Direct numerical simulation (DNS) is used to investigate the role of shear instabilities in turbulent mixing in a model of the upper Equatorial Undercurrent (EUC). The background flow consists of a westward-moving surface mixed layer above a stably stratified EUC flowing to the east. An important characteristic of the eastward current is that the gradient Richardson number Ri_g is larger than $1/4$. Nevertheless, the overall flow is unstable and DNS is used to investigate the generation of intermittent bursts of turbulent motions within the EUC region where $\mathrm{Ri}_g > 1/4$. In this model, an asymmetric Holmboe instability emerges at the base of the mixed layer, moves at the speed of the local velocity, and ejects wisps of fluid from the EUC upward. At the crests of the Holmboe waves, secondary Kelvin–Helmholtz instabilities develop, leading to three-dimensional turbulent motions. Vortices formed by the Kelvin–Helmholtz instability are occasionally ejected downward and stretched by the EUC into a horseshoe configuration creating intermittent bursts of turbulence at depth. Vertically coherent oscillations, with wavelength and frequency matching those of the Holmboe waves, propagate horizontally in the EUC where the turbulent mixing by the horseshoe vortices occurs. The oscillations are able to transport momentum and energy from the mixed layer downward into the EUC. They do not overturn the isopycnals, however, and, though correlated in space and time with the turbulent bursts, are not directly responsible for their generation. These wavelike features and intermittent turbulent bursts are qualitatively similar to the near-*N* oscillations and the deep-cycle turbulence observed at the upper flank of the Pacific Equatorial Undercurrent.

1. Introduction

The Pacific Equatorial Undercurrents (EUCs) occur in a dynamically rich regime of stratified shear flows. Zonal winds, large-scale pressure gradients, and surface buoyancy flux conspire to create a sheared, jetlike current within a depth-varying stratification characterized by a surface mixed layer overlying strong, stable stratification below. Of particular interest are the vertical exchange of heat and momentum within the stratified waters below the base of the mixed layer, the mechanisms by which these fluxes are maintained, and their dynamical link with processes within and at the base of the mixed layer.

Several field experiments, for example, TROPIC HEAT, TROPIC HEAT 2, and Tropical Instability Wave Experiment (TIWE), have revealed the frequent occurrence of intermittent turbulent bursts (deep-cycle turbulence) well below the surface mixed layer, usually during the night. The turbulent bursts are energetic, with kinetic energy dissipation rates that are often three orders of magnitude greater than those measured outside the patches (Gregg et al. 1985; Peters et al. 1988; Moum et al. 1992; McPhaden and Peters 1992; Lien et al. 2002). The occurrence of turbulent bursts is strongly correlated with the presence of narrowband near-*N* oscillations, for example, Moum et al. (2011). To illustrate, Fig. 1a, taken from Moum et al. (2011), shows the typical coincidence of energetic turbulent patches and near-*N* oscillations of the isotherms. The dynamical link between the near-*N* oscillations and the turbulent patches, however, is not yet well understood and is one of the central themes of the present work.

There appear to be two main hypotheses in the literature regarding the energy source for the observed deep-cycle turbulence. The two hypotheses differ with respect to the energetic significance of the near-*N* oscillations. In the first, see, for example, Lien et al. (1996),

Corresponding author address: Hieu T. Pham, Department of Mechanical and Aerospace Engineering, University of California, San Diego, 9500 Gilman Dr., La Jolla, CA 92092.
E-mail: h8pham@ucsd.edu

DOI: 10.1175/JPO-D-11-0233.1

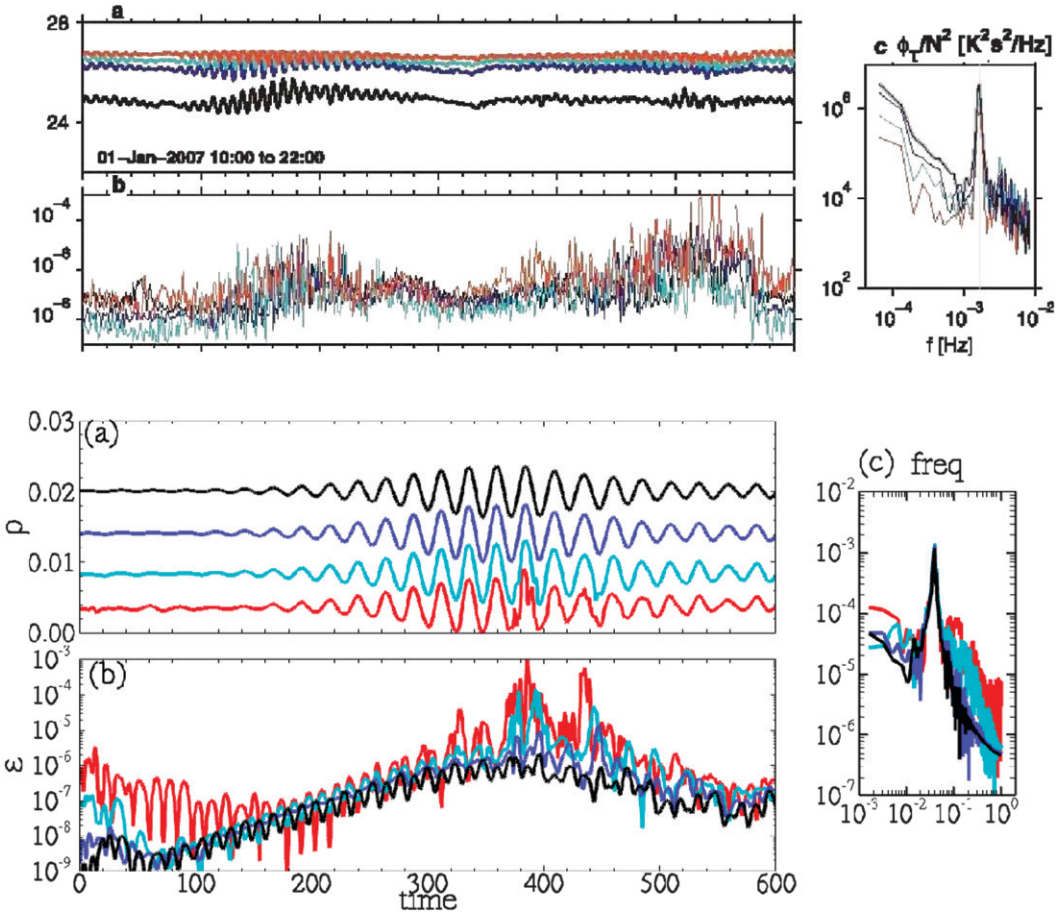

FIG. 1. Qualitative similarity between (top) observations of Moum et al. (2011) and (bottom) our model. (top) Observation: (a) temperature signals (°C) at 29- (red), 39- (cyan), 49- (blue), and 59-m (black) depths; (b) scalar dissipation rate (m^2 s^{-3}) at corresponding depths; (c) temperature spectra normalized by the mean value of N at that depth. (bottom) Our model: (a) density at 0.6- (red), 0.8- (cyan), 1.0- (blue), and 1.2-m (black) depths in the upper flank of the model EUC; (b) turbulent dissipation rate at corresponding depths; and (c) frequency spectra of the density records in (a).

Lien et al. (2002), and Moum et al. (2011), the sheared region is seen as generally stable, with a gradient Richardson number larger than ¼ over time scales on the order of a day, but subject to higher frequency variability that acts to intermittently increase the shear and/or decrease the stratification well below the base of the mixed layer. Such events are capable of extracting energy from the undercurrent that drives the growth of wavelike modes with frequencies of order N that displace the isotherms over a finite vertical region. If the gradient Richardson number is small enough, the growth rate of these modes can be large enough that they grow to finite amplitude and evolve into turbulent Kelvin–Helmholz billows. These are the ''deep'' modes of shear instability discussed by Smyth et al. (2011). In this scenario, the turbulent billows are responsible for the observed bursts and the energy source is the kinetic energy of the shear flow at the depth of the observed turbulence. The near-N oscillations represent an energy loss to the process: some of the energy extracted from the ambient shear is radiated as internal waves with the remainder available to drive the small-scale turbulent dissipation and mixing. That growing modes of shear instability radiates energy away from the region of minimum gradient Richardson number is well-known from three-dimensional studies of turbulent billows (Pham et al. 2009) and also from stability analyses and two-dimensional simulations of EUC-like flows (Sutherland 1996; Sun et al. 1998; Smyth and Moum 2002). One observed turbulent event, where both towed thermistor chain and microstructure profile data were available (Hebert et al. 1992), appears consistent with this hypothesis. The background stratification profile obtained prior to the event shows a localized minimum in N at a depth of about 55 m, just above the

velocity maximum of the EUC where the shear is not particularly strong.

The second hypothesis is that near-N wavelike disturbances are generated at the base of the mixed layer, either by the largest-scale turbulent motions within the mixed layer itself or by shear instabilities just beneath the base of the mixed layer (Moum et al. 1989; Wijesekera and Dillon 1991; Skyllingstad and Denbo 1994; Wang and Muller 2002). These waves then propagate downward and eventually break owing to the influence of the relatively strong shear of the undercurrent below. Under this hypothesis, the gradient Richardson number of the EUC itself need never fall below ¼ at the depths where the turbulent bursts occur. The energy source here is the energy driving the wavelike disturbances themselves, which could be surface buoyancy fluxes, winds, the kinetic energy of the undercurrent near the base of the mixed layer, or a combination of these sources. Shear instabilities originating near the base of the mixed layer are labeled as ''shallow'' modes in the Smyth et al. (2011) study.

In this investigation, we use three-dimensional direct numerical simulation (DNS) to provide insight to the nonlinear evolution of a ''shallow'' shear instability in a simplified model of the upper EUC. The DNS model has dimensions that are scaled down with respect to the EUC while preserving the structural aspects of the measured velocity and stratification profiles. Results from this model, shown in Fig. 1b, show both wavelike motions as well as intermittent, spatially localized turbulent bursts well below the mixed layer where the ambient shear is stable. Though the process is initiated by a shear instability near the base of the mixed layer, which we call the primary instability, the flow evolution is not as envisioned in the second hypothesis discussed above. As the instability grows, energy is radiated to depth in the form of propagating near-N waves but these waves do not overturn and break. Rather, instabilities near the base of the mixed layer undergo secondary instabilities that intermittently eject horseshoe vortices and turbulent bursts into the upper flank of the EUC, which is always characterized by $\mathrm{Ri}_g > ¼$. The primary instability itself, however, is not localized to the base of the mixed layer even though the amplitude of the fastest growing eigenfunction does indeed have a local maximum there. The eigenfunction decays with depth but is nonzero in the sheared EUC flank. When the primary instability reaches finite amplitude, it is characterized by local overturns near the base of the mixed layer and finite amplitude but nonoverturning wavelike oscillations below. We will show that the frequency and horizontal scale of these oscillations, if scaled up to EUC dimensions, are in reasonable agreement with those observed in the Pacific EUC. These wavelike motions are able to radiate energy downward but only to a finite turning depth, below which the waves become evanescent.

We will make all of these arguments more precisely in the body of this work. In section 2, we describe the model setup and the numerical method. In section 3, we describe the evolution of the primary Holmboe-like instability, the wavelike oscillations and the turbulent bursts. In section 4, we compare the oscillations in our EUC model to near-N oscillations in previous observational data. Finally, in section 5 we modify hypothesis two above to describe the evolution of the nonlinear flow subsequent to the instability of a ''shallow'' mode and propose a new mechanism for the generation of deep-cycle turbulence that does not rely on overturns of the near-N oscillations as an energy source.

2. Model formulation

a. Flow conditions

We choose background velocity and density profiles similar to the previous measurements reported in Moum et al. (2011). We model the westward surface current and the upper-flank of the EUC as two opposing streams with a velocity difference ΔU and half-thickness δ_ω as shown in Fig. 2a. At the surface $z = 0$, the velocity is directed westward toward the negative x direction. At depth $z = -\delta_\omega$, the velocity changes sign denoting the eastward undercurrent. The maximum shear rate S occurs at the depth $z = -\delta_\omega$. The depth of the maximum eastward velocity is $2\delta_\omega$ and the velocity difference between this maxima and flow speed at the surface is ΔU. For the observed profiles of Moum et al. (2011), these scales are approximately 100 m and 2 m/s corresponding to $2\delta_\omega$ and ΔU, respectively. We assume the effects of any ambient meridonal flow to be negligible. We will perturb the background flow and simulate the nonlinear evolution over a time scale of a few hours. This is longer than the observed time scales of the near-N oscillations and the turbulent bursts but not long enough to model the diurnal cycle of a surface mixed layer due to wind stress and surface heat flux.

The specified background density field is shown in Fig. 2a. It consists of a surface mixed layer overlying a linearly stratified layer. The corresponding profile for the squared buoyancy frequency N^2 is shown in Fig. 2b. At the surface, N^2 is equal to zero in accordance with a well-mixed surface layer. At depth $z \approx -0.5\delta_\omega$, N^2 increases over a half-thickness of δ_N because of the presence of the thermocline. For specificity, we define the depth at which N^2 is equal to half of that in the EUC as the base of the surface mixed layer, located at $z = -0.75\delta_\omega$. The ambient gradient Richardson number $\mathrm{Ri}_g(z)$ shown in Fig. 2c has

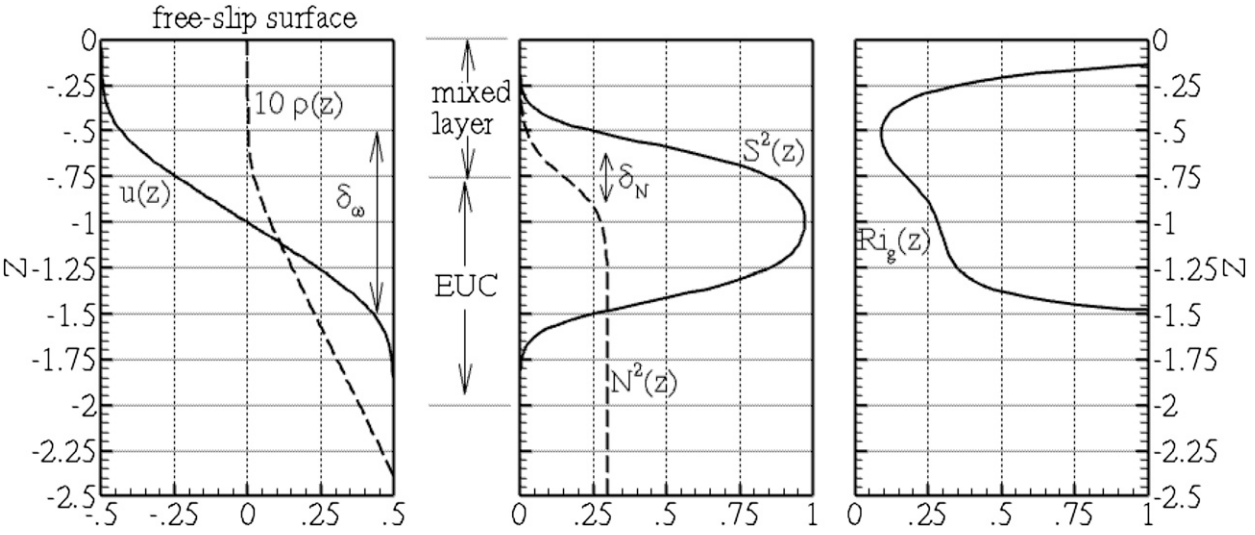

FIG. 2. Initial mean profiles. The velocity consists of a surface current (SEC) moving westward in an opposite direction to an underlying current (EUC) with a velocity difference ΔU and a half-thickness δ_ω. The maximum shear is at $z = -\delta_\omega$ in the EUC. The density variation corresponds to a hyperbolic tangent profile in the squared buoyancy frequency $N^2(z)$. At the base of the mixed layer, $z = -0.75\delta_\omega$, $N^2(z)$ transitions from an upper mixed layer to a linearly stratified lower region over a half-thickness δ_N. The gradient Richardson number Ri_g is less than 0.25 in the surface mixed layer and larger than 0.25 in the EUC.

a minimum value of approximately 0.1 in the surface mixed layer at $z = -0.5\delta_\omega$ and increases with depth. There is a thin region of $\mathrm{Ri}_g < 0.25$ between the surface mixed layer and the EUC ($-0.9 < \delta_\omega < -0.75$) where a shear instability can grow. The value of Ri_g at the depth of maximum shear is larger than 0.25 because of the relatively large N^2 at that depth. Field measurements reported in Moum et al. (1992), Lien et al. (2002), and Moum et al. (2011) show similar profiles of Ri_g in the upper flank of the EUC. In particular, the prescribed Ri_g profile resembles the conditions for ''shallow'' mode shear instability of Smyth et al. (2011).

b. Mathematical model

We seek numerical solutions for velocity $\mathbf{u}$ and density ρ for the Navier–Stokes equations under the Boussinesq approximation in a nonrotating Cartesian physical space with zonal direction x, meridional direction y and vertical direction z:

$$\frac{\partial \mathbf{u}}{\partial t} + (\mathbf{u}\cdot\nabla)\mathbf{u} = -\nabla p' + \frac{1}{\mathrm{Re}}\nabla^2\mathbf{u} - J_d\rho'\mathbf{k}; \quad \text{and} \quad (1)$$

$$\nabla\cdot\mathbf{u} = 0. \quad (2)$$

We have nondimensionalized using the velocity difference ΔU and current thickness δ_ω. Let ρ be the deviation from a constant characteristic density ρ_0. Then

$$\frac{\partial \rho}{\partial t} + (\mathbf{u}\cdot\nabla)\rho = \frac{1}{\mathrm{RePr}}\nabla^2\rho. \quad (3)$$

In the last term of Eq. (1) ρ' is the fluctuating density defined as the deviation from the value averaged in the zonal x and meridional y directions, that is, $\rho'(x, y, z) = \rho(x, y, z) - \langle\rho\rangle(z)$ where the brackets denote the x–y average. The pressure in Eq. (1) is the corresponding fluctuating pressure. Primes and brackets to denote fluctuating and mean quantities, respectively, will be used extensively in our discussion. Furthermore, all results will be presented in dimensionless form.

The nondimensional parameters in the governing equations are the Reynolds number $\mathrm{Re} = \Delta U\delta_\omega/\nu$, the Richardson number $J_d = N_d^2\delta_\omega^2/\Delta U^2$, and the Prandlt number $\mathrm{Pr} = \nu/\kappa$. Here ν is kinematic viscosity, κ is the thermal diffusivity, and N_d^2 is the value of the ambient N^2 in the linearly stratified layer at depth. The values used in our DNS are $\mathrm{Re} = 5000$, $J_d = 0.3$, and $\mathrm{Pr} = 7$ While the use of DNS allows us to avoid a turbulent mixing parameterization, our Re is approximately four orders of magnitude smaller than the corresponding value for the EUC. Nevertheless, we interpret our simulated flow as a ''moderately high Re'' flow because both the primary and secondary instabilities that we observe have growth rates sufficiently large that the time scales of instability are significantly shorter than the viscous decay times corresponding to their observed length scales. In this sense, inertial effects dominate viscous effects at the scales of the instabilities and we have a ''moderately high Re'' turbulent flow. The qualifier ''moderate'' is used to indicate that, particularly for the secondary instability, though the time scales are distinct, they are not different

by several orders of magnitude. Implicit in this interpretation is the assumption that the instabilities are the rate controlling process and that these motions are only weakly influenced by our low Re. We hypothesize that at larger Re, the dynamics of the instabilities and thus the dissipation rates remain essentially the same but the turbulence itself is characterized by a much wider inertial subrange.

c. Initial conditions

The flow conditions shown in Fig. 2 correspond to the following shear and stratification profiles:

$$S(z) = \frac{1}{2}\left[-\tanh\left(\frac{z+0.5}{0.2}\right) + \tanh\left(\frac{z+1.5}{0.2}\right)\right], \quad (4)$$

and

$$N^2(z) = \frac{J_d}{2}\tanh\left(\frac{z+0.75}{0.2}\right), \quad (5)$$

respectively. Small-amplitude fluctuating velocities with a specified spectrum are added to perturb the background flow. The spectral content of the fluctuations has the following form:

$$E(k) = \left(\frac{k}{k_0}\right)^4 \exp\left[-2\left(\frac{k}{k_0}\right)^2\right], \quad (6)$$

where k_0 is set such that the spectrum peaks at 1.7. The fluctuations are focused at the base of the surface mixed layer with the following function for the rms:

$$A\exp\left(\frac{z+0.75}{0.2}\right), \quad (7)$$

where A is the amplitude of the fluctuations with magnitude of 0.1% ΔU.

d. Boundary conditions

We assume horizontal periodicity. All flow variables f thus satisfy

$$f(x,y,z) = f(x+L_x,y,z) = f(x,y+L_y,z), \quad (8)$$

where L_x and L_y are the lengths of the simulated domain in the zonal and meridional directions, respectively. At the surface $z = 0$, free-slip conditions are used on the horizontal velocities u and v, along with an adiabatic condition on density ρ,

$$\left.\frac{\partial u}{\partial z}\right|_{z=0} = \left.\frac{\partial v}{\partial z}\right|_{z=0} = \left.\frac{\partial \rho}{\partial z}\right|_{z=0} = 0. \quad (9)$$

The upper surface is a free-slip rigid lid and so

$$w|_{z=0} = 0. \quad (10)$$

At the lower boundary, similar conditions are used on the velocities while a constant flux matching the ambient density gradient is prescribed for density

$$\left.\frac{\partial \rho}{\partial z}\right|_{z=0} = -J_d. \quad (11)$$

We employ a sponge layer in the region $-L_z < z < -10$, which actively damps all fluctuating quantities toward their respective boundary values. The sponge layer suppresses the reflection of any internal waves that reach the bottom boundary.

e. Numerical methods

The governing equations [Eqs. (1)–(3)] are integrated in time using an implicit second-order Crank–Nicolson scheme for viscous and diffusive terms in the vertical direction and an explicit third-order Runge–Kutta scheme for other terms. Time step is determined by a Courant–Freidrichs–Lewy (CFL) stability condition. Second-order finite-difference spatial discretization is employed in all three directions and the pressure is computed using a multigrid Poisson solver. The computational grid is staggered as the density and the pressure are defined at cell centers and the velocities are defined at cell faces. The code is run in parallel using the message passing interface protocols. For further discussions on the code, we refer the readers to Basak and Sarkar (2006) and Brucker and Sarkar (2007).

The computational domain has a zonal length L_x equal to $16/3\pi$ and a meridional length L_y equal to $4/3\pi$ and a depth L_z equal to 19.6, discretized by 768, 192, and 192 grid points, respectively. The grid is uniform in the horizontal directions with a spacing of 0.021. In the vertical direction, the grid is uniform in the region between the surface and depth $z = -1.5$ below which the spacing is stretched at 3% ratio. The grid, with spacing of only a few times the Batchelor scale, has sufficient resolution to resolve the scales of shear instability, internal waves, and turbulence observed in our model.

3. Model results

The evolution of the simulated flow begins with growth of a Holmboe-like shear instability near the base of the mixed layer. Oscillations of the isopycnals with frequency close to N are produced at depth as a direct consequence of the growing instability. The oscillations are vertically

coherent and propagate westward at the speed and in the direction of the flow at the base of the mixed layer, that is, upstream with respect to the EUC core. In time, the instability grows to finite amplitude and induces a secondary Kelvin–Helmholtz (KH) shear instability, which causes patches of intense turbulence both at the base of the mixed layer and in the EUC. Vortices associated with the overturns of the KH billows are occasionally ejected downward and stretched into a horseshoe configuration by the shear of the EUC jet. The ejections create localized patches of turbulence in the EUC core where the ambient gradient Richardson number is larger than 0.25. In this section, the spatial evolution of these phenomena is described. In section 4 and 5, the temporal evolution is analyzed and compared to mooring data presented in previous literature.

Background conditions where the shear region is significantly thicker than the density transition layer and the stratification is significant favor the emergence of a Holmboe instability rather than a KH instability as discussed by Alexakis (2005, 2009) and Carpenter et al. (2010). The Holmboe instability appears as a wave traveling with respect to the mean and, during its nonlinear evolution, the wave crests steepen into cusplike features. We show below, through density contours, that the initial evolution in the present flow has the characteristics of a Holmboe instability. In section 4, results of a linear stability analysis will be given to show that the most unstable mode is of the Holmboe type and not the KH type.

The density fields in Figs. 3a,b show the development of the shear instability. At $t = 150$, the isopycnals near the base of the mixed layer show two crests at approximately $x = 4.5$ and $x = 13$. The instability has a wavelength λ_x equal to 8.4, corresponding to a horizontal wavenumber $k_x = 0.75$ and a phase speed of -0.33 where the negative sign indicates propagation in negative x direction. The instability emerges at $z = -0.75$. Smyth et al. (2011) refer to this depth as a critical level because the local velocity $\langle u \rangle$ is equal to the phase speed of the growing mode. We denote this depth here simply as the level of instability to differentiate it from a singular critical level as seen for example in Winters and D'Asaro (1994). Although both studies refer to the level at which the local velocity and the phase speed have the same value, extraction of energy from the mean flow occurs in the former while deposition of wave energy occurs in the latter. Similar to the ''shallow'' modes of Smyth et al. (2011) the instability level occurs at the base of the mixed layer in our simulation. At $t = 322$, the crests of the growing Holmboe waves evolve into cusplike structures where wisps of heavy fluid are ejected upward in the counterclockwise direction. Such ejections are characteristic of the nonlinear evolution of Holmboe instabilities (Smyth and Winters 2003; Carpenter et al. 2007). The vertical displacement of the isopycnals originating near the base of the mixed layer are substantial, with the tip of the wisps reaching up to $z = -0.2$. Though the wisps produce overturns in the density field, the density contrast within the overturns is small. This behavior is also characteristic of finite-amplitude Holmboe instabilities and contrasts with the finite-amplitude behavior of KH billows. The isopycnals below $z = -1$ in the EUC core also exhibit oscillatory motions. These oscillations are vertically coherent with the wavelength and phase speed equal to that of the Holmboe instability. The oscillations grow in amplitude at the same rate as the Holmboe instability at the base of the mixed layer and have the same horizontal scale. These oscillations, however, neither form wisps nor directly break into turbulence; they remain oscillatory in space and time. In the discussion that follows, we refer to the growing mode as a Holmboe instability to emphasize that it grows at the expense of the shear flow at the base of the mixed layer and that its characteristics are predictable via linear stability analysis. One might also call this mode a growing Holmboe wave because it propagates horizontally and radiates energy vertically.

The nonlinear development of the Holmboe instability induces a secondary KH shear instability as shown in Figs. 3c,d. When the amplitude of the Holmboe instability becomes sufficiently large, the secondary instability grows rapidly and causes the isopycnals to roll up into overturning billows that collapse into small-scale three-dimensional turbulent motions. The horizontal scale of the secondary shear instability is significantly smaller than the horizontal scale of the Holmboe waves. At $t = 367$, three overturning billows are seen on the crest of the Holmboe wave at $x = 13$. The overturns have counterclockwise rotation, which is in the same sense as the spanwise y vorticity of the background shear. The vertical extent of the overturns is significantly smaller than the wavelength of the Holmboe instability. The overturns are advected westward in the negative x direction at the phase speed of the Holmboe instability. The Kelvin–Helmholtz instability only occurs at the base of the mixed layer but not below $z = -1$ in the EUC. The weaker stratification at the base of the mixed layer is less able to suppress overturns of finite scale. Nevertheless, localized turbulence appears within the EUC as shown in Fig. 3d at $t = 414$ at $x = 2$ and $z = -1.2$. This turbulence is caused by a vortex that originates from the overturns at the base of the mixed layer and penetrates into the EUC below. We elaborate further on this turbulence generation mechanism in section 5 and relate it to the deep-cycle turbulence in field observations.

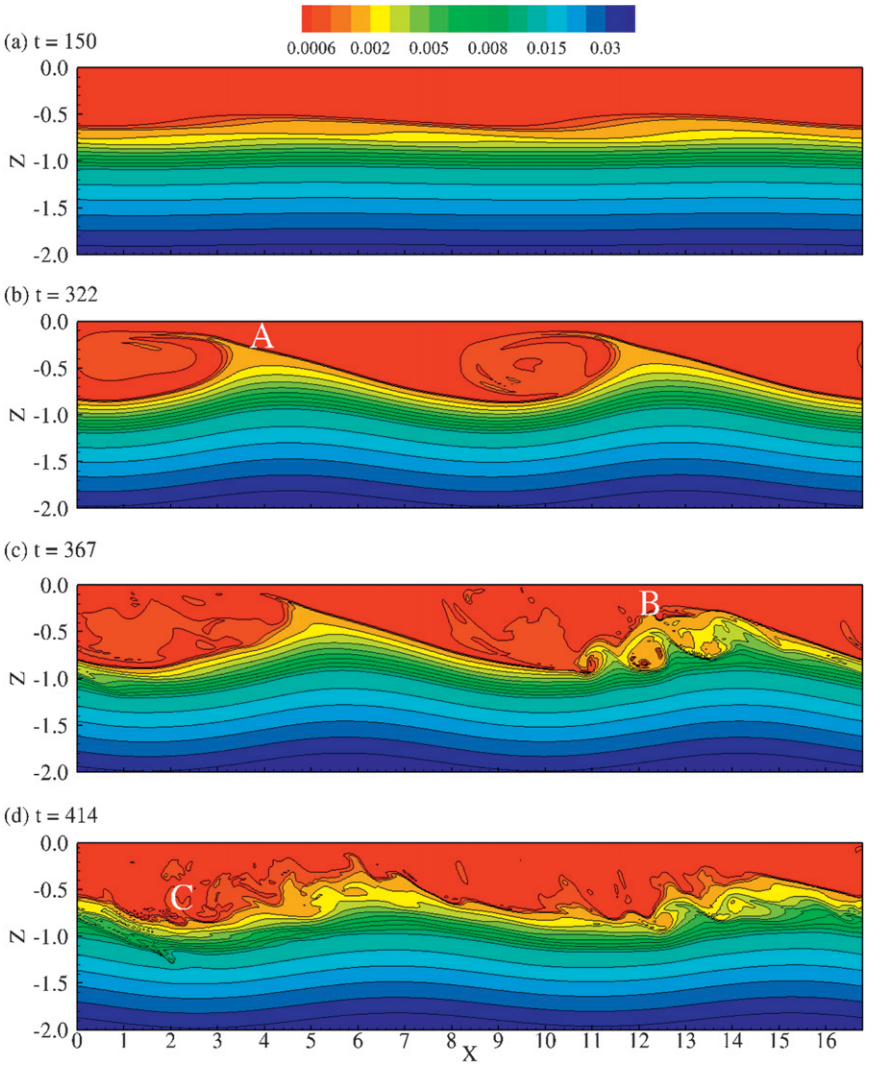

FIG. 3. Snapshots of the density fields ρ at $y = 313$ show the evolution of the Holmboe instability and the secondary Kelvin–Helmholtz shear instability. (a) Holmboe instability grows at the base of the mixed layer. (b) Wisps of fluid from the EUC are ejected upward into the mixed layer and isopycnals in the EUC show spatial oscillations. (c) Billows form at the crest of the Holmboe instability at $x = 13$. (d) The billows break down and local mixing are seen in the EUC, as deep as $z = -1.2$. The westward (leftward)-moving Holmboe wave crest denoted by A gives rise to the Kelvin–Helmholtz shear instability at B, which subsequently breaks down to turbulence at C.

The secondary KH shear instability results from the enhancement of vorticity by the primary Holmboe instability. The growth of the Holmboe instability creates a horizontal gradient in the vertical velocity $\partial w/\partial x$ along a distorted isopycnal. In the upslope region (leftward face of the crest) of the isopycnal, $\partial w/\partial x$ is positive so that the total vorticity $\partial u/\partial z - \partial w/\partial x$ is larger in magnitude (more negative) than the mean vorticity. In the downslope region, $\partial w/\partial x$ is negative and the net vorticity is smaller than the mean vorticity so that overturns are less likely.

The vorticity associated with the KH billows generates significant turbulence below the mixed layer as indicated by the dissipation rate ε shown in Fig. 4. Patches of strong dissipation occur at $t = 367$ corresponding to the billows at the crests of the Holmboe instability. They are advected westward at the speed of the Holmboe instability and the dissipation rate inside the patches is up to three orders of magnitude larger than that outside the patch in the EUC. In Fig. 4b at $t = 414$, the downward stretching of vortices (due to the background shear in the EUC) creates a localized burst of strong dissipation at

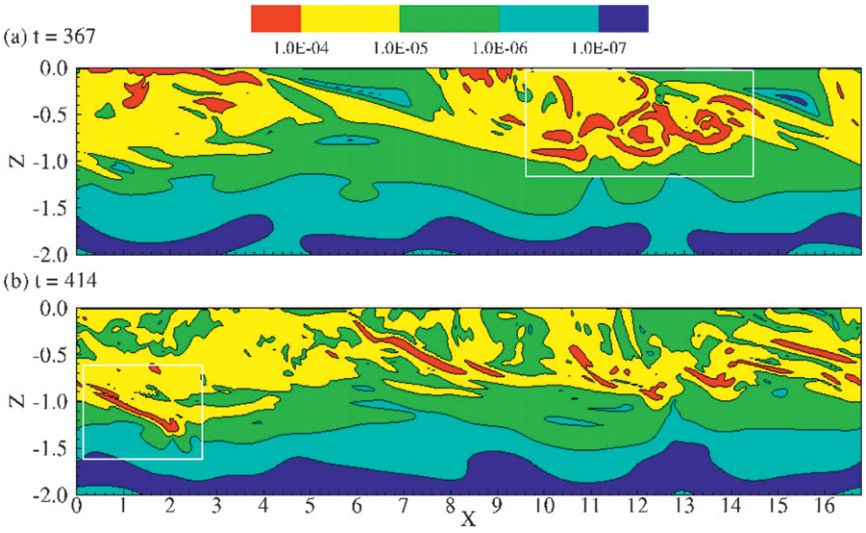

FIG. 4. Snapshots of the dissipation field ε at $y = 3.13$. (a) Elevated dissipation rates (in box) surround the Kelvin–Helmholtz billows seen in Fig. 3c. (b) A localized patch of high dissipation rate (in box) extends from the base of the surface mixed layer into the EUC.

$x = 2$ and $-1.2 < z < -1$. The turbulence burst occurs well within the EUC where large-amplitude oscillations of the isopycnals are also present and the horizontally averaged gradient Richardson is larger than 0.25. Comparing Fig. 3d to Fig. 4b, we see that the oscillations of the isopycnals and the localized patches of turbulence inside the EUC are strongly correlated in time. We have shown, however, that the former does not directly cause the latter. The enhanced dissipation results from the formation of vortices by the secondary KH instability at the base of the mixed layer and the penetration of these vortices into the EUC.

The growth of Holmboe instability transfers energy from the mean flow at the base of the mixed layer to the fluctuating fields. The profiles of mean velocity $\langle u \rangle$ at different times shown in Fig. 5a indicate that the velocity magnitude, and hence the mean kinetic energy, in the surface layer decreases in time. The change in the velocity below $z = -1$ in the EUC is insignificant and is mostly due to molecular viscous diffusion indicating that the EUC at depth is not an energy source for the observed fluctuations. Rather, the energy extracted from the mean flow at the base of the mixed layer drives the growth of both the local wisp-like structures as well as

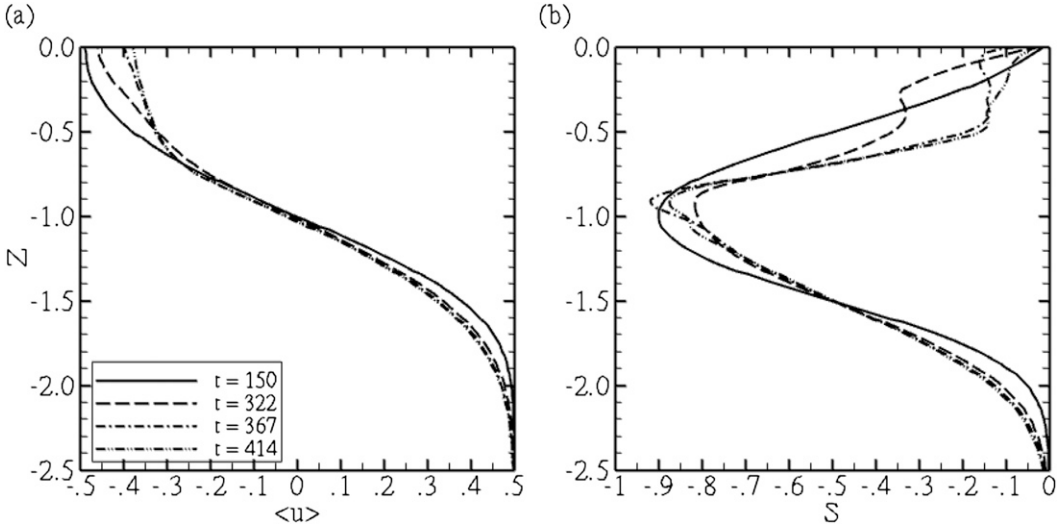

FIG. 5. Profiles of mean velocity $\langle u \rangle$ and shear S at various times.

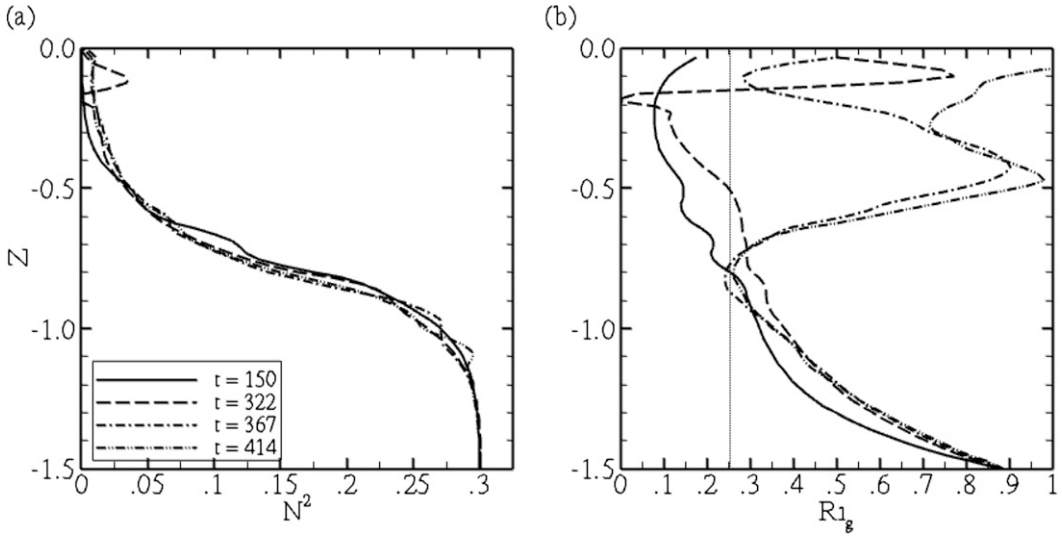

FIG. 6. Profiles of (a) squared buoyancy frequency N^2 and (b) gradient Richardson number Ri_g at various times. The dotted line in (b) indicates the critical value for linear shear instability.

the near-N isopycnal oscillations with matching phase speed and horizontal scale below. The Holmboe mode itself extracts energy from the instability level and transports it downward into the EUC region where the mean kinetic energy is not significantly changed. Similarly, the profiles of mean shear rate S at various times in Fig. 5b indicate significant change only in the surface layer. In the EUC, the change in shear rate is less even though the oscillations grow to finite amplitude in this region.

The evolution of the background stratification is shown in Fig. 6a. In the surface layer, N^2 increases because of the ejections of heavy fluid upward by the Holmboe instability. At the base of the mixed layer, N^2 decreases slightly while in the EUC region below it remains constant. Insignificant variation in the background stratification, however, does not imply that no mixing has occurred. Indeed, we have observed bursts of energetic turbulence in this region. These bursts, although strong, are intermittent and localized so that, when averaged over the entire horizontal extent of the model domain, their net effect on the background density is small. Profiles of Ri_g are shown in Fig. 6b. Between $t = 150$ and $t = 322$, as the Holmboe instability grows to large amplitude, the Ri_g increases to a value greater than ¼ in the EUC. By $t = 322$, Ri_g has fallen below ¼ in a thin region near $z = -0.8$, where the secondary KH instability develops. Throughout the simulation, Ri_g remains greater than ¼ in the region below $z = -1$. We emphasize, however, that the Ri_g in this figure is a horizontally averaged value that includes only the vertical shear ($\partial u/\partial z$). A modified Richardson number $\mathrm{Ri}_{g,m}$, for which the shear of the oscillations ($\partial w/\partial x$) is included, does attain values less than ¼ in the region below $z = -1$ just before the appearance of the KH billows. A comparison of instantaneous Ri_g and $\mathrm{Ri}_{g,m}$ is shown in Fig. 7.

4. Near-N oscillations

The energy source for the near-N oscillations has been a prevalent component of the discussion of the EUC for many years. One view suggests that the oscillations are internal waves excited by the dynamics (shear instabilities, convective overturns, etc.) at the base of the mixed layer that propagate downward into the EUC core (Wijesekera and Dillon 1991; McPhaden and Peters 1992; Skyllingstad and Denbo 1994). A second view suggests that they are related to occasional shear instabilities that occur locally inside the EUC itself (Sun et al. 1998; Lien et al. 2002; Smyth et al. 2011). The first interpretation suggests that wave momentum and energy originate in the surface mixed layer while the second implies that they are extracted locally from the mean flow in the EUC. Whether the energy source is shallow or deep and whether the energy of the oscillations represents a source or a sink to the process or processes driving deep turbulent bursts is significant if we wish to parameterize the resulting vertical fluxes. In this section, we show that our simulation suggests that the narrowband, near-N oscillations in the EUC could be linked to a Holmboe instability that develops at the base of the mixed layer. We also show that the oscillations produced by this mechanism transport energy from the base of the mixed layer downward into the EUC.

Some previous studies of the EUC have invoked linear stability analysis to explain the origin of the near-N

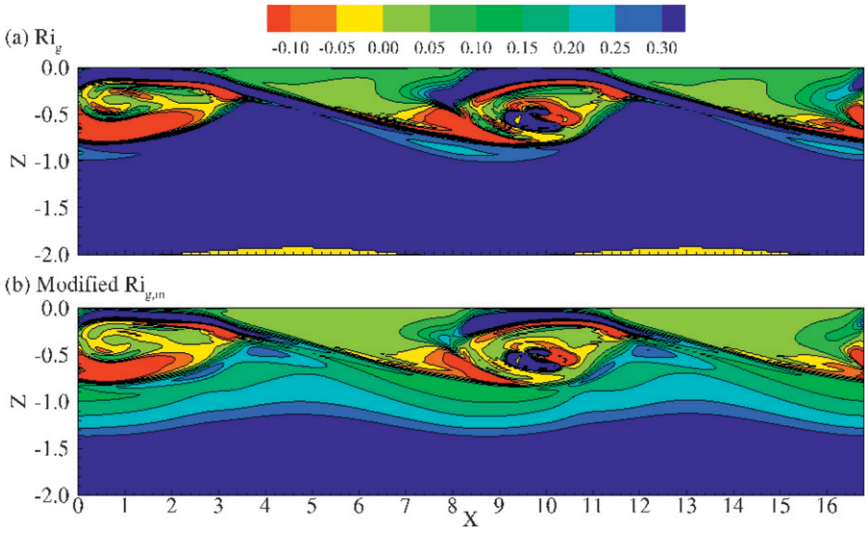

FIG. 7. (a) Instantaneous gradient Richardson number; (b) modified gradient Richardson number with the contribution of $\partial w/\partial x$ at a time corresponding to Fig. 3b.

oscillations (Sutherland 1996; Sun et al. 1998; Smyth and Moum 2002; Smyth et al. 2011). Such an analysis yields the growth rate, the horizontal wavelength, the frequency, and the shape of the vertical eigenfunction corresponding to the fastest growing mode of instability given a background velocity and stratification profile. A shear instability can extract energy from the background shear at an instability level and transport the energy to regions far from the instability level, depending on the shape of the eigenfunctions. For example, the linear stability analysis of Sun et al. (1998) based on observational data from TIWE indicates that small disturbances can extract energy from the mean flow of the EUC and redistribute it over large vertical extent. Finite-amplitude disturbances can thus occur in regions far from the instability level, a location where the phase speed of the instability is equal to the local velocity. Similarly, the analysis of Smyth et al. (2011) using the most recent observational data also shows the vertical profile of the energy flux extends far away from the instability level and that, consequently, the redistribution of energy in the vertical is as important as the extraction of energy at the instability level.

We perform a similar linear stability analysis on the initial profiles of velocity and stratification used in our simulation. The magnitude of the eigenfunctions for the zonal velocity $\hat{u}$, the vertical velocity $\hat{w}$, and the buoyancy $\hat{b} = -J_d\hat{\rho}$ corresponding to the fastest growing mode are plotted in Fig. 8a. All eigenfunctions are normalized by the peak value of $\hat{w}$. At the instability level $z = -0.75$, $\hat{u}$ and $\hat{b}$ have local maxima while $\hat{w}$ peaks much deeper within the EUC. All eigenfunctions extend far away from the instability level suggesting that the instability in our model is capable of radiating energy to deep within the stratified EUC. The rms values of the corresponding quantities at $t = 200$ from the simulation plotted in Fig. 8 show qualitative agreement between the linear stability analysis and the direct numerical simulation. We conclude therefore that the oscillations in our modeled EUC are a direct result of the Holmboe instability generated at the base of the mixed layer. Still at issue is the subsequent nonlinear evolution of the fluctuations initially described by these eigenfunctions and their relationship to the observed turbulent mixing. Specifically, we ask whether turbulence can be expected over the entire vertical extent of the eigenfunctions of the fastest growing mode or is it confined to the vicinity of the instability level? While linear stability analysis suggests the energy source and the vertical distribution of the near-N oscillations, it cannot address the finite-amplitude evolution of the flow nor the pathway to turbulence.

Figure 9 shows x–t diagrams of the simulated density at two different depths in the EUC to show the relationship between the wavelength and the frequency of the oscillations. The figures on the left are the x–t diagrams while those on the right show the corresponding spectra in wavenumber k_x and frequency ω space. At both depths, the oscillations propagate westward (the negative x direction) at the same speed since the slope of the phase lines is the same in the x–t diagrams. The spectra show a peak at $|k_x| = 0.75$ and $\omega = 0.25$, which is approximately half of the local buoyancy frequency N. The wave phase speed is therefore $\omega/k_x = -0.33$, taking the negative value of k_x for westward propagating waves.

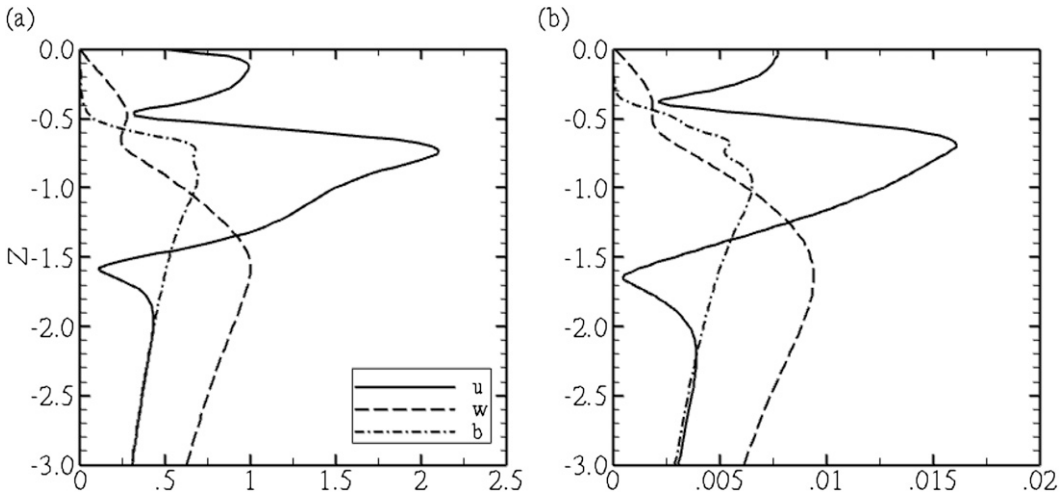

FIG. 8. Profiles of (a) eigenfunctions from linear stability analysis and (b) rms values from DNS at $t = 200$ of zonal velocity u', vertical velocity w', and buoyancy $b' = -J_d\rho'$.

To demonstrate the wavelike characteristics of the oscillations in the EUC, we examine the coefficient Q^2 in the Taylor–Goldstein equation governing the eigenfunction $\hat{w}$:

$$\frac{d^2\hat{w}}{dz^2} + Q^2(z)\hat{w} = 0,$$

where,

$$Q^2(z) = \frac{N^2}{[\omega/k_x - \langle u\rangle(z)]^2} + \frac{d^2\langle u\rangle/dz^2}{[\omega/k_x - \langle u\rangle(z)]} - k_x^2. \tag{12}$$

Figure 10a shows a vertical profile of Q^2 computed using the wavelength and the apparent frequency of the oscillations in combination with the initial background flow condition. Here, Q^2 is positive in the EUC, $-2.0 < z < -0.75$. It has a maximum value equal to 4.25 suggesting the shortest vertical wavelength is equal to $2\pi/Q \approx 3$. The thickness of the EUC, equal to 1.25, is significantly smaller than one complete vertical wavelength. In our model, both velocity and density vary rapidly in the EUC and thus propagating internal waves with clear phase line are not expected. The oscillations in the EUC are the tail of the Holmboe instability that emerges at the base of the mixed layer. The fact that Q^2 is positive in this region suggests that the fastest growing mode is wavelike at these depths. The mode carries momentum and energy from the base of the mixed layer downward into the EUC. Energy is reflected upward at the turning level $z \approx 2$ where $Q^2 = 0$. Figure 10b shows the energy flux $\langle p'w'\rangle$ carried by these oscillations at different times. At $t = 322$, the negative $\langle p'w'\rangle$ indicates a downward energy flux into the EUC. Later, $\langle p'w'\rangle$ changes sign indicating a net upward flux due to reflection and the weakening of rate of shallow energy extraction once the mode becomes fully developed. Below the turning depth, the amplitude of the oscillations decays and there are no downward fluxes. Momentum and energy are thus trapped within the EUC.

For a direct comparison with the observations, we scale up our model assuming the simulated flow is approximately Reynolds number independent. When the surface current at $z = 0$ is assumed to flow westward at a speed of -1.0 m s^{-1} and the maximum velocity of the EUC jet is 1.0 m s^{-1}at depth, ΔU in our model is equal to 2.0 m s^{-1}. Taking the depth of the maximum eastward velocity to be 100 m in the observations, δ_ω in our model is equal to 50 m. These scales fall within the range of the observations of Moum et al. (1992), Lien et al. (2002), and Moum et al. (2011). Our simulated oscillations correspond to a frequency 8×10^{-4} Hz. The near-N spectra in Moum et al. (2011) peaks at 1–2 $\times 10^{-3}$ Hz while the value in Moum et al. (1992) and Lien et al. (2002) is 0.01 Hz. The wavelength in our model scales to 420 m with a westward phase speed of 0.6 m s^{-1} while the estimated wavelength from Moum et al. (1992) is between 150–250 m with a phase speed of 0.1 m s^{-1}. The corresponding values from Lien et al. (2002) are 360 m and 0.5 m s^{-1}, respectively. Noting the variability of the EUC background conditions between observations, the values obtained by scaling up our DNS results are consistent with the observational data.

5. Deep-cycle turbulence

Previous studies show a strong correlation between near-N oscillations and deep-cycle turbulence in the EUC

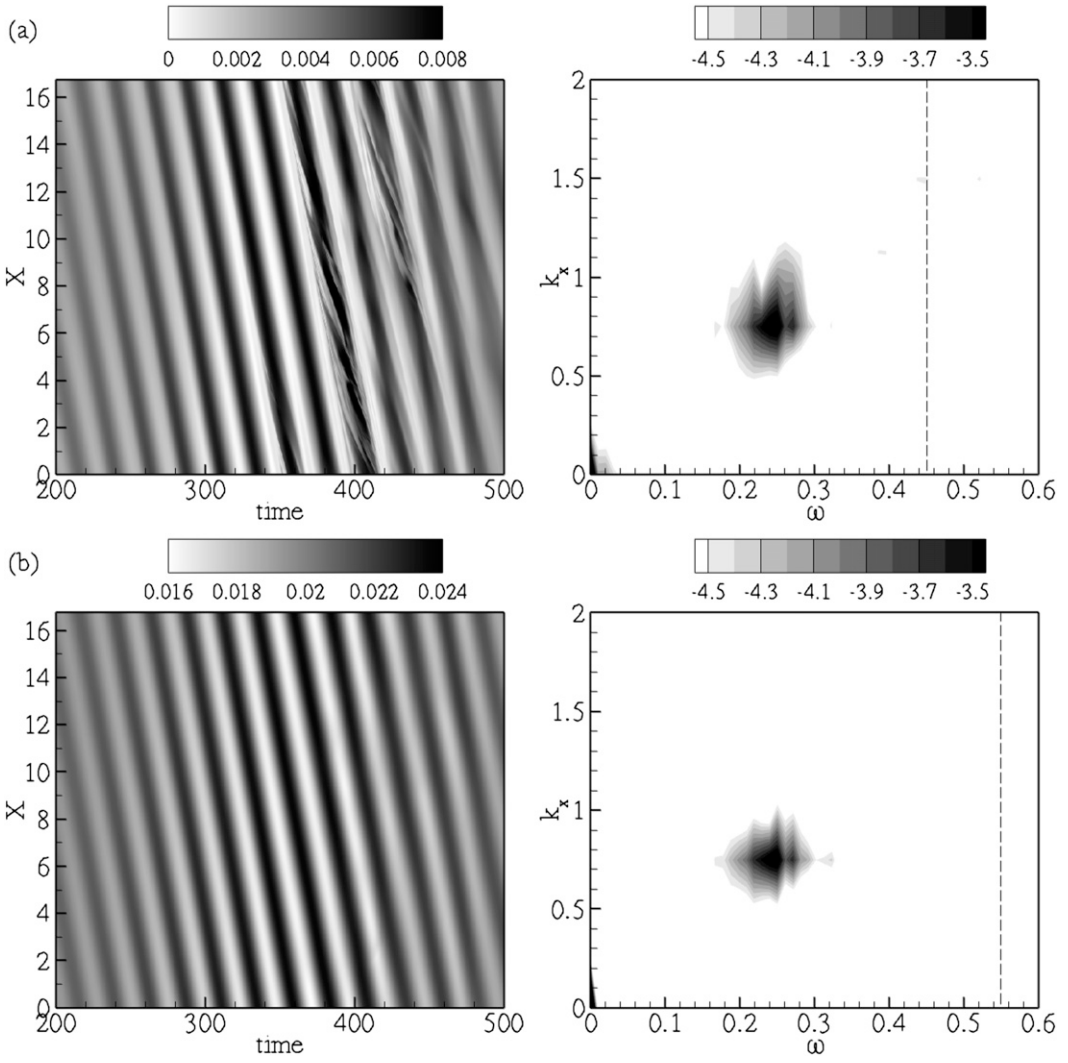

FIG. 9. Spectral analysis on the $x - t$ density fields at different depths yields the following: $k_x = -0.75$, $\omega = 0.25$, and the phase speed $c = \omega/k_x = -0.33$. Data are taken at $y = 0.31$ and (a) $z = -0.8$ and (b) $z = -1.4$. Vertical dashed lines in figures to the right indicate buoyancy frequency N.

(Gregg et al. 1985; Moum et al. 1992; Lien et al. 1996; Moum et al. 2011). With the notable exception of Hebert et al. (1992) and Lien et al. (2002), however, detailed observations of the processes leading to the mixing events themselves are not available. In this section we examine the formation of turbulent patches with high dissipation rates in the context of the primary and secondary instabilities and the near-N oscillations in our DNS model.

Figure 11 shows the evolution of the instantaneous turbulent dissipation rate along a fixed vertical pencil. The white solid lines are isopycnals showing the near-N oscillations. The temporal correlation between the oscillations and the dissipation rate is evident. The turbulent dissipation rate during the initial growth of the Holmboe instability at the base of the mixed layer, that is, between about $t = 100$ and $t = 300$, is small. The highest dissipation rates are induced by the secondary Kelvin–Helmholtz billows at about $t = 380$. Patches of strong turbulence extend below the level at which the billows occur, reaching as deep as $z = -1.2$, within the stably stratified EUC. The dissipation rate in these patches is three orders of magnitude larger that the corresponding value at this depth at earlier times. By $t = 380$, the isopycnals at the base of the mixed layer are steep but not overturned.

We compare the simulated event with the evolution of a single wave packet described in Hebert et al. (1992). The observed packet had five crests and six troughs with a frequency of 0.01 Hz. The middle crest appeared to overturn creating a patch of elevated dissipation rate in the depth range 40–70 m. The dissipation rate of the

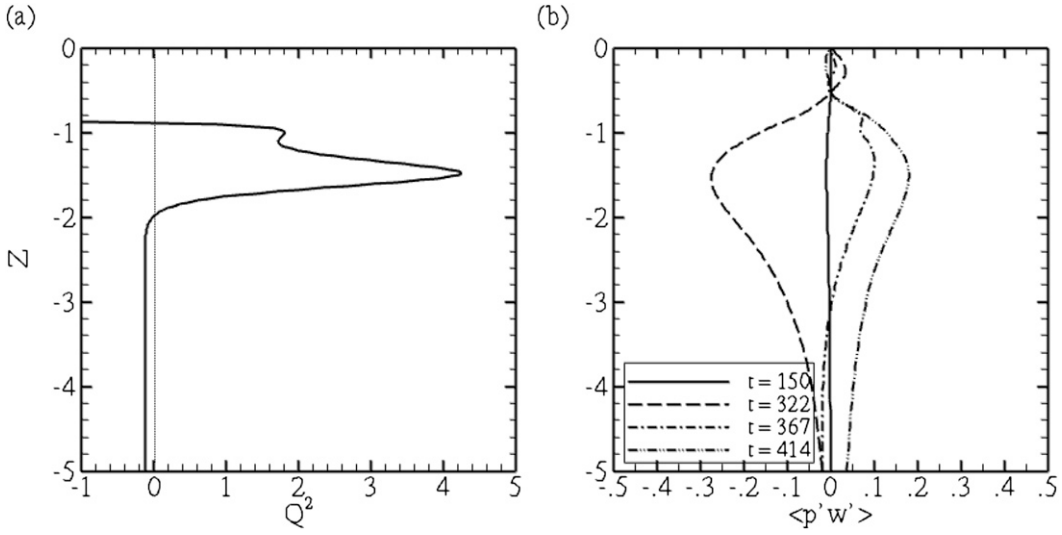

FIG. 10. Profiles of (a) Q^2 at $t = 0$ and (b) wave energy flux $\langle p'w' \rangle$ at various times. The oscillations carry energy from the instability level downward and are reflected upward at the turning level where $Q^2 = 0$.

patch was 2.2×10^{-5} m^2 s^{-3}, at least three orders of magnitude larger than outside the patch at the same depth. Based on the observed properties of the packet, the overturning wave crest was suggested to be unstable to both advective instability and wave-induced shear instability. The isopycnals from the simulation, shown in Fig. 11, also exhibit large-amplitude oscillations with the steepest wave distortion occurring at $t = 360$. Different from Hebert et al. (1992), however, Fig. 11 does not show that steepened isopycnals overturn and directly energize the turbulent patches. Rather, the finite-amplitude Holmboe waves undergo secondary shear instabilities. As the isopycnals steepen, the local shear is enhanced by lateral gradients of the vertical velocity, the modified gradient Richardson number is reduced, and a secondary Kelvin–Helmholtz instability is rapidly initiated. The subsequent evolution of these billows lead to localized overturns and turbulent bursts. Our model thus suggests a turbulence generation mechanism that does not require the near-N oscillations at depth to steepen to the point of overturning. Since the Holmboe waves, that nonlinearly evolve through secondary instabilities to turbulence, themselves draw their energy from the shear flow at the base of the mixed

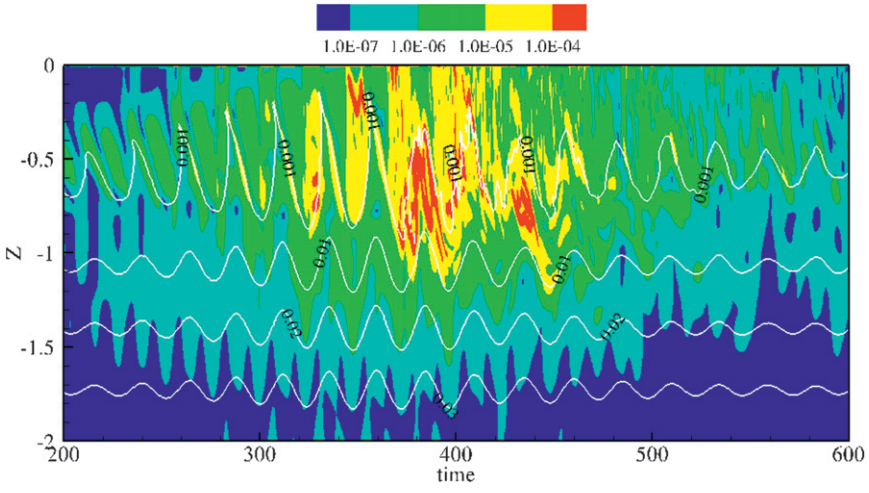

FIG. 11. Temporal evolution of the vertical profile of density and dissipation rate ε at $x = 8.4$ and $y = 3.1$. White solid lines are isopycnals. Patches of intense turbulence occur in the EUC where the horizontally-averaged Ri_g is larger than 0.25. The dissipation rate inside the patches is up to three orders of magnitude outside the patches.

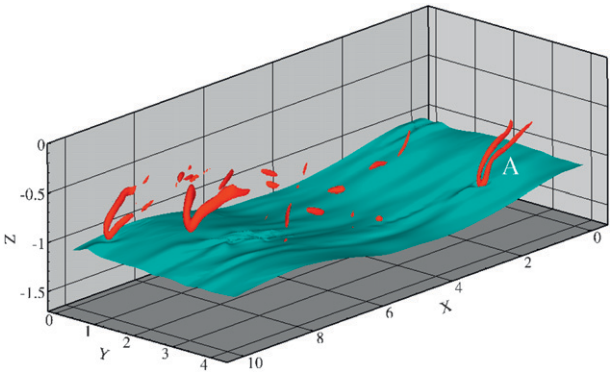

FIG. 12. Coherent horseshoe vortex structures and internal waves at $t = 409$. The blue isopycnal surface shows the structure of the oscillations. The red isosurfaces of λ_2 depict the formation of the horseshoe vortices. The spanwise vortices associated with the Kelvin–Helmholtz billows are stretched into the horseshoe vortices by the EUC shear. These horseshoe vortices are responsible for the enhanced turbulence in the EUC. The structure denoted by A generates the turbulence in the boxed region in Fig. 4b.

layer, the turbulent processes at depth have remote, shallow energy sources.

Frequently, the vortices produced by the secondary KH instabilities are stretched downward beneath their depth of generation as shown in Fig. 12. Shown in red is an isosurface of λ_2, a quantity typically used to accurately define vortex cores (Jeong and Hussain 1995). As the vortices are ejected downward, they are stretched into the horseshoe shape by the EUC shear. In a simulation of a stratified jet motivated by the EUC, Pham and Sarkar (2010) have shown a similar generation of the horseshoe vortices. In that simulation, however, the oscillations due to the Holmboe instability were absent.

Other mechanisms are also possible. Though the observational data indicates that the daily averaged Ri_g within the EUC is greater than 1/4; it has been suggested that hourly averaged values can be smaller and so "deep" mode shear instabilities at depth are possible (Lien et al. 2002; Moum et al. 2011). Recently, Smyth et al. (2011) analyzed hourly averaged profiles of velocity and density over a 54-day interval and showed that 334 profiles are susceptible to shear instability according to a linear viscous stability analysis. Of those, 182 are labeled as "shallow" modes with instability levels in the surface mixed layer. Our simulation suggests that such "shallow" modes can create turbulent bursts at depth by initiating first a Holmboe instability at the base of the mixed layer, followed by a secondary KH instability and an ejection of horseshoe vorticies.

6. Conclusions

In the present study, we have performed simulations with a numerical model initialized with shear and stratification profiles similar to those seen in the EUC. As the flow evolves, instability at the base of the surface mixed layer produces a train of Holmboe waves with a westward horizontal phase speed matching that of the local mean current. The vertical eigenfunctions associated with the unstable Holmboe waves have a local maximum near the base of the mixed layer but have nonzero amplitude at depth, that is, within the EUC itself. At these depths, the unstable modes produce a flow signature characterized by vertically coherent, near-N oscillations. These oscillations are wavelike in that they carry momentum and energy from the base of the mixed layer downward until they encounter a turning level near the location of the maximum velocity of the EUC jet where they are reflected upward.

As the Holmboe instability grows to finite amplitude at the base of the mixed layer, that is, roughly when the Holmboe waves begin to eject wisps of dense fluid into the mixed layer, a secondary shear instability is excited. Kelvin–Helmholtz billows grow to finite amplitude and produce overturns and turbulent patches near the crests of the Holmboe waves. Vortices associated with these billows are occasionally ejected downward into the EUC where they are stretched into a horseshoe configuration by the EUC shear and lead to localized patches of strong dissipation within the EUC where the long-time-averaged gradient Richardson number is larger than 1/4. The dissipation rate within these ejection events is at least three orders of magnitude larger than that before the ejection and is qualitatively consistent with EUC observations. At the end of the turbulent mixing events, the value of Ri_g exceeds 0.25 for all z and the Holmboe instability decays.

The near-N oscillations in our simulation are signatures of a Holmboe instability produced at the base of the mixed layer where the local Ri_g is less than 1/4. Scaling our results to the EUC, that is, taking the distance from the surface to the depth of maximum eastward velocity in the EUC core to be approximately 100 m and the velocity difference across this region to be 2 m/s, yields a wavelength and wave period for these features of 420 m and 20.8 min, respectively. Smyth et al. (2011) suggested that the wavelength of the near-N oscillations should be approximately 7 times the half thickness of an occasionally unstable shear layer in the EUC core yielding a substantially shorter wavelength of 140 m. The wavelength in our model depends on the Holmboe instability whose wavelength is equal to (in this particular case) 8.3 times the half-thickness between the surface and the depth of maximum eastward velocity of the EUC jet. When the jet is shallower, shorter wavelengths are expected. As the oscillations in the EUC region of our model are intrinsically linked to the

Holmboe instability at the base of the mixed layer, their excitation mechanism and energy source are fundamentally different than those associated with generation via occasional shear instability within the EUC itself.

While the near-N oscillations and the deep-cycle turbulence are coincident in our modeled EUC, overturns of the near-N oscillations themselves are not observed. Instead, secondary KH instabilities and ejection and stretching of horseshoe vortices produce deep, isolated patches of turbulence characterized by high dissipation rates. This generation mechanism does not directly depend on a small Ri_g within the EUC itself and so turbulence patches are produced there even when the mean value of Ri_g in the EUC is larger than 1/4. The key to this mechanism is the generation of spanwise vortices at the base of the mixed layer just above the EUC shear. Though the shear in the EUC is not strong enough to overcome the stratification and drive local instabilities, it appears to play an important role in the downward ejections and stretching of the horseshoe vortices. The study of Pham and Sarkar (2010) has shown in detail that vortices associated with Kelvin–Helmholtz billows can be ejected downward into a sheared region with Ri_g larger than 1/4 in a similar manner. Pham and Sarkar (2011) further show that vortices associated with the deepening of a turbulent mixed layer can also be ejected into the lower stratified water column. When a spanwise vortex emerges at the base of the mixed layer, downward ejection and stretching by the EUC shear are likely. The penetration depth of the ejections and the turbulent intensity of the patches depend on the size and the strength of the spanwise vortices as well as the magnitude of the shear and the stratification in the EUC.

Our model introduces the Holmboe instability and the ejections of the horseshoe vortices into the discussion of the dynamics inside the EUC system. While previous studies (Smyth et al. 1988; Smyth and Winters 2003; Alexakis 2009; Carpenter et al. 2010) have considered the growth and nonlinear evolution of Holmboe instabilites, this instability has not previously been linked to the observations of the EUC. Similarly, though vortex ejections have not been observed in the field, many high-resolution numerical simulations show ejections of coherent vortex structures under different flow conditions (Enstad et al. 2006; Wu and Moin 2009). We suggest that the dynamics exhibited in these simulations lead to flow signatures that are similar to observations of deep-cycle turbulence in the EUC.

We conclude with a few caveats regarding the interpretation of these results. First, we stress that the evolution of the shear instabilities in our model are based on idealized profiles of the shear rate and stratification. The specific idealized profiles are chosen for the study are based on time averaged background flow conditions observed in the EUC, guided by linear stability analysis for stratified shear flows. Our model does not include dynamics associated with wind and diurnal heat flux. Finally, our model is a DNS of a sequence of processes that we suggest will occur similarly at much higher Re. We argue explicitly that our relatively low Re is sufficiently high that inertial (nonlinear) effects dominate viscous effects at the spatial scales of the growing instabilities. Moreover, the horizontal scales of the simulated Holmboe modes of instability are those expected based on linear stability theory. This suggests that the sequence of instabilities and the scales at which they occur would be the same for higher Re flows. We expect that the main effects of the relatively low Re to be a significantly reduced inertial subrange and a smearing of the dynamics at scales smaller than that of the secondary KH instability.

Acknowledgments. We are grateful for the support provided by NSF 0961184 and program monitor E. Itsweire.

REFERENCES

Alexakis, A., 2005: On Holmboe's instability for smooth shear and density profiles. *Phys. Fluids,* **17,** 84–103.

——, 2009: Stratified shear flow instabilities at large Richardson numbers. *Phys. Fluids,* **21,** 54–108.

Basak, S., and S. Sarkar, 2006: Dynamics of a stratified shear layer with horizontal shear. *J. Fluid Mech.,* **568,** 19–54.

Brucker, K., and S. Sarkar, 2007: Evolution of an initially turbulent stratified shear layer. *Phys. Fluids,* **19,** 101–105.

Carpenter, J. R., G. A. Lawrence, and W. D. Smyth, 2007: Evolution and mixing of asymmetric Holmboe instabilities. *J. Fluid Mech.,* **582,** 103–132.

——, E. W. Tedford, M. Rahmani, and G. A. Lawrence, 2010: Holmboe wave fields in simulation and experiment. *J. Fluid Mech.,* **648,** 205–223.

Enstad, L. I., R. Nagaosa, and G. Alendal, 2006: Low shear turbulence structures beneath stress-driven interface with neutral and stable stratification. *Phys. Fluids,* **18,** 55–106.

Gregg, M. C., H. Peters, J. C. Wesson, N. S. Oakey, and T. J. Shay, 1985: Intensive measurements of turbulence and shear in the Equatorial Undercurrent. *Nature,* **314,** 140–144.

Hebert, D., J. Moum, C. Paulson, and D. Caldwell, 1992: Turbulence and internal waves at the equator. Part II: Details of a single event. *J. Phys. Oceanogr.,* **22,** 1346–1356.

Jeong, J., and F. Hussain, 1995: On the identification of a vortex. *J. Fluid Mech.,* **285,** 64–94.

Lien, R.-C., M. McPhaden, and M. Gregg, 1996: High-frequency internal waves at 0°, 140°W and their possible relationship to deep-cycle turbulence. *J. Phys. Oceanogr.,* **26,** 581–600.

——, E. D'Asaro, and M. McPhaden, 2002: Internal waves and turbulence in the upper central equatorial Pacific: Lagrangian and Eularian observations. *J. Phys. Oceanogr.,* **32,** 2619–2639.

McPhaden, M., and H. Peters, 1992: Diurnal cycle of internal wave variability in the equatorial Pacific ocean: Results from moored observations. *J. Phys. Oceanogr.,* **22,** 1317–1329.

Moum, J. N., D. Caldwell, and C. Paulson, 1989: Mixing in the equatorial surface layer and thermocline. *J. Geophys. Res.,* **94** (C2), 2005–2021.

——, D. Hebert, C. Paulson, and D. Caldwell, 1992: Turbulence and internal waves at the equator. Part I: Statistics from towed thermistors and a microstructure profiler. *J. Phys. Oceanogr.,* **22,** 1330–1345.

——, J. D. Nash, and W. D. Smyth, 2011: Narrowband oscillations in the upper equatorial ocean. Part I: Interpretation as shear instabilities. *J. Phys. Oceanogr.,* **41,** 397–410.

Peters, H., M. Gregg, and J. Toole, 1988: On the parameterization of equatorial turbulence. *J. Geophys. Res.,* **93** (C2), 1199–1218.

Pham, H. T., and S. Sarkar, 2010: Internal waves and turbulence in a stable stratified jet. *J. Fluid Mech.,* **648,** 297–324.

——, and ——, 2011: Mixing events in a stratified jet subject to surface wind and buoyancy forcing. *J. Fluid Mech.,* **685,** 54–82.

——, ——, and K. A. Brucker, 2009: Dynamics of a stratified shear layer above a region of uniform stratification. *J. Fluid Mech.,* **630,** 191–223.

Skyllingstad, E., and D. Denbo, 1994: The role of internal gravity waves in the equatorial current system. *J. Phys. Oceanogr.,* **24,** 2093–2110.

Smyth, W. D., and J. Moum, 2002: Shear instability and gravity wave saturation in an asymmetrically stratified jet. *Dyn. Atmos. Oceans,* **35,** 265–294.

——, and K. B. Winters, 2003: Turbulence and mixing in Holmboe waves. *J. Phys. Oceanogr.,* **33,** 694–711.

——, G. P. Klaassen, and W. R. Peltier, 1988: Finite amplitude Holmboe waves. *Geophys. Astrophys. Fluid Dyn.,* **43,** 181–222.

——, J. N. Moum, and J. D. Nash, 2011: Narrowband oscillations at the upper equatorial ocean. Part II: Properties of shear instabilities. *J. Phys. Oceanogr.,* **41,** 412–428.

Sun, C., W. D. Smyth, and J. Moum, 1998: Dynamic instability of stratified shear flow in the upper equatorial Pacfic. *J. Geophys. Res.,* **103,** 10 323–10 337.

Sutherland, B. R., 1996: Dynamic excitation of internal gravity waves in the equatorial ocean. *J. Phys. Oceanogr.,* **26,** 2398–2419.

Wang, D., and P. Muller, 2002: Effects of equatorial undercurrent shear on upper-ocean mixing and internal waves. *J. Phys. Oceanogr.,* **32,** 1041–1057.

Wijesekera, H., and T. Dillon, 1991: Internal waves and mixing in the upper equatorial Pacific ocean. *J. Geophys. Res.,* **96** (C4), 7115–7125.

Winters, K. B., and E. A. D'Asaro, 1994: Three-dimensional wave instability near a critical layer. *J. Fluid Mech.,* **272,** 255–284.

Wu, X., and P. Moin, 2009: Direct numerical simulation of turbulence in a nominally zero-pressure-gradient flat-plate boundary layer. *J. Fluid Mech.,* **630,** 5–41.